LETTER

Moving magnetoencephalography towards real–world applications with a wearable system

Elena Boto[1]*, Niall Holmes[1]*, James Leggett[1]*, Gillian Roberts[1]*, Vishal Shah[2], Sofie S. Meyer[3,4], Leonardo Duque Muñoz[3], Karen J. Mullinger[1,5], Tim M. Tierney[3], Sven Bestmann[3,6], Gareth R. Barnes[3]§, Richard Bowtell[1]§ & Matthew J. Brookes[1]§

Imaging human brain function with techniques such as magnetoencephalography[1] typically requires a subject to perform tasks while their head remains still within a restrictive scanner. This artificial environment makes the technique inaccessible to many people, and limits the experimental questions that can be addressed. For example, it has been difficult to apply neuroimaging to investigation of the neural substrates of cognitive development in babies and children, or to study processes in adults that require unconstrained head movement (such as spatial navigation). Here we describe a magnetoencephalography system that can be worn like a helmet, allowing free and natural movement during scanning. This is possible owing to the integration of quantum sensors[2,3], which do not rely on superconducting technology, with a system for nulling background magnetic fields. We demonstrate human electrophysiological measurement at millisecond resolution while subjects make natural movements, including head nodding, stretching, drinking and playing a ball game. Our results compare well to those of the current state-of-the-art, even when subjects make large head movements. The system opens up new possibilities for scanning any subject or patient group, with myriad applications such as characterization of the neurodevelopmental connectome, imaging subjects moving naturally in a virtual environment and investigating the pathophysiology of movement disorders.

Magnetoencephalography[1] (MEG) allows direct imaging of human brain electrophysiology by measurement of magnetic fields generated at the scalp by neural currents. Mathematical analysis of those fields enables the generation of 3D images that show the formation and dissolution of brain networks in real time. MEG measurements of brain activity are currently made using an array of superconducting sensors placed around the head[1,4]. These cryogenically cooled sensors have femtotesla (fT) sensitivity, which is needed to detect the weak magnetic fields produced by the brain. Unfortunately, the requirement
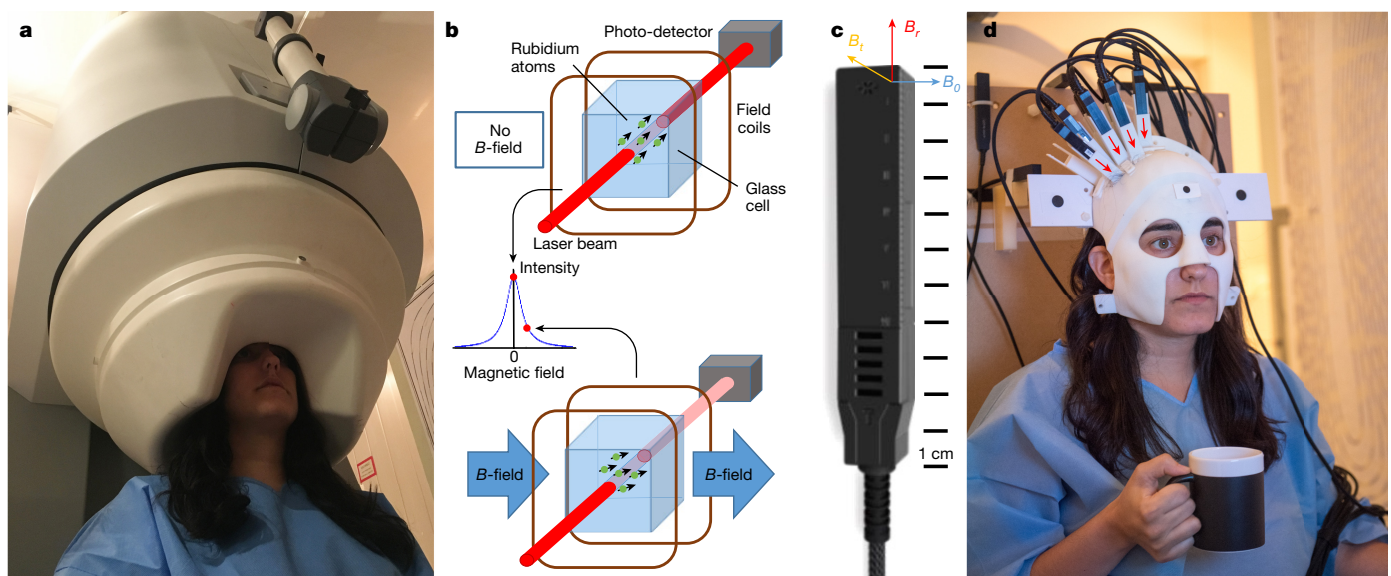

Figure 1 | A new generation of MEG system. a, A conventional 275-channel cryogenic MEG system. Weighing about 450 kg, the system is fixed and cumbersome and subjects must remain still relative to the fixed sensor array. **b,** Schematic illustration of zero-field resonance in an OPM sensor. Top, operation in zero-field; bottom, Larmor precession when an external field (*B*-field) impinges on the cell and the transmitted light intensity is reduced. **c,** A commercial OPM sensor made by QuSpin. The geometry used is illustrated by the coloured axes where B_r is the radial field component, B_t the tangential field component and B_o the direction along which the laser beam is oriented. **d,** Our prototype OPM-MEG system helmet. The helmet weighs 905 g and is customized so that the sensors (which in this prototype cover only the right sensorimotor cortex) are directly adjacent to the scalp surface. The subject is free to move their head. The measured radial field direction for the sensors is illustrated by the red arrows.

[1]Sir Peter Mansfield Imaging Centre, School of Physics and Astronomy, University of Nottingham, University Park, Nottingham NG7 2RD, UK. [2]QuSpin Inc., 331 South 104th Street, Suite 130, Louisville, Colorado 80027, USA. [3]Wellcome Centre for Human Neuroimaging, UCL Institute of Neurology, University College London, 12 Queen Square, London WC1N 3BG, UK. [4]Institute of Cognitive Neuroscience, University College London, 17–19 Queen Square, London WC1N 3AZ, UK. [5]Centre for Human Brain Health, School of Psychology, University of Birmingham, Edgbaston, Birmingham B15 2TT, UK. [6]Sobell Department for Motor Neuroscience and Movement Disorders, UCL Institute of Neurology, University College London, Queen Square House, Queen Square, London WC1N 3BG, UK.
*These authors contributed equally to this work.
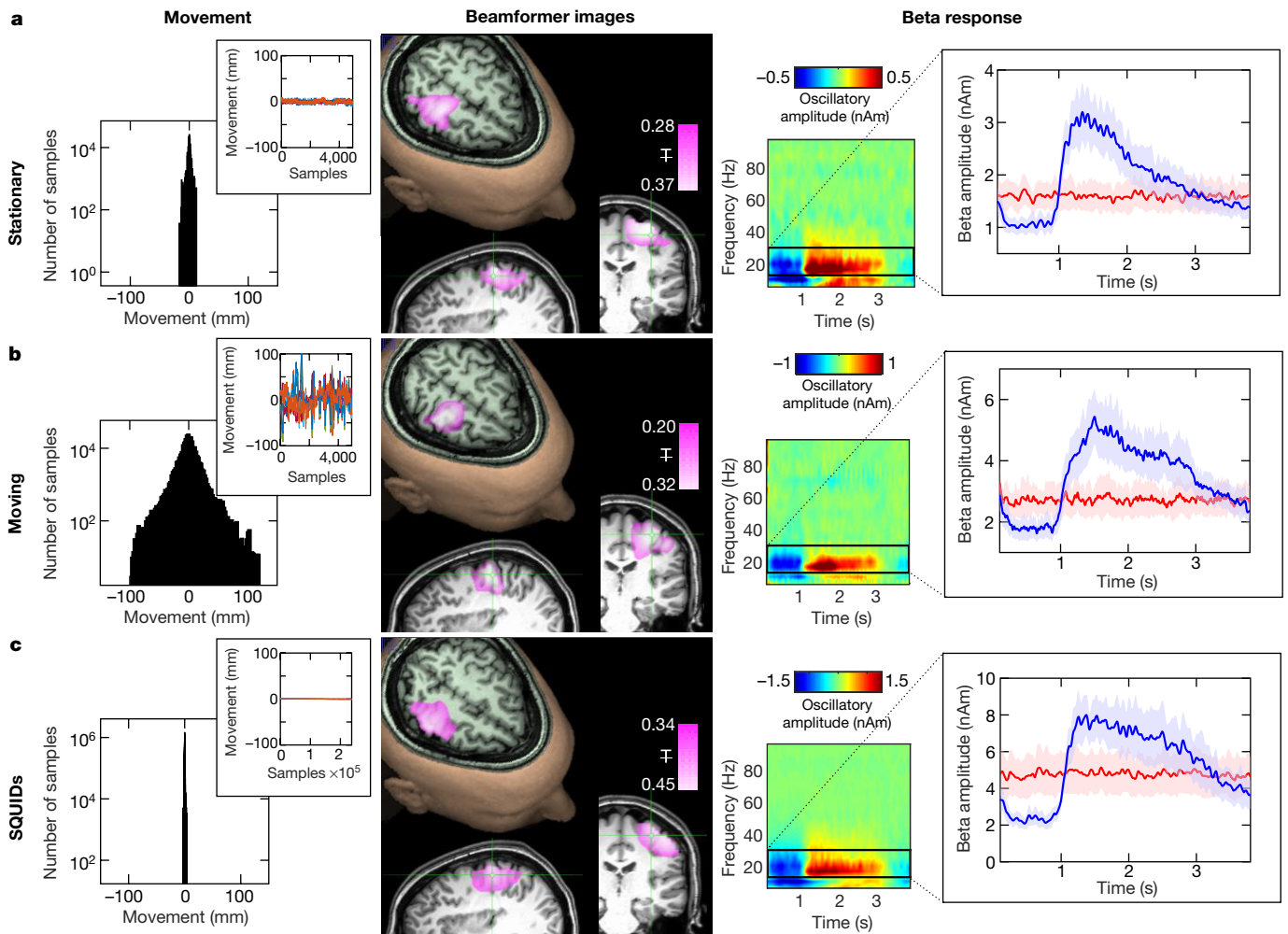§These authors jointly supervised this work.

Figure 2 | OPM-MEG results. a, Results when the subject was asked to remain still. **b**, Results when the subject was moving. **c**, Data collected using a cryogenic MEG instrument (SQUIDs) for comparison. In each row, the left panel contains a histogram showing movement of three fiducial markers on the subject's head. The inset graph shows the change in marker positions over a typical experiment; different colours show movement in three Cartesian axes of the three markers. The middle panel shows the change in beta band power due to finger abduction (pink) overlaid onto axial, sagittal and coronal slices of the anatomical MRI. The functionally active region overlays contralateral sensorimotor cortex. In the right panel, a time–frequency spectrogram depicts changes in neural oscillations during finger abduction. The inset graph shows the characteristic beta band response for finger abduction (blue) and rest trials (red). In all cases the results are averaged over trials and experiments and the shaded region shows s.e. over six experiments. SIR ranged from 4.3 to 8.2 for static OPM measures, 4.2 to 5.8 for moving OPMs and 4.9 to 7.9 for the cryogenic system. Further analysis (Extended Data Fig. 2 and Supplementary Information section 2) showed that the OPM system outperformed the cryogenic system in terms of both spatial resolution and robustness across experiments. Temporal resolution was quantified at 130 Hz.

for cooling means that sensors must be housed within a liquid helium dewar with a vacuum space separating sensors from the scalp. MEG systems are therefore cumbersome (Fig. 1a) and sensor positions are fixed in a one-size-fits-all helmet. Any motion of the head relative to the sensors reduces data quality markedly: even a 5-mm movement can prevent use of the data[5]. Further, the brain-to-sensor distance, which is substantial in adults (about 3 cm), is increased markedly in subjects with small heads, reducing the available signal because the magnetic field decreases with the square of the distance between the source and the sensor. These characteristics make participation in MEG studies challenging for many subject groups, including infants and many patients. They also make the MEG scanner environment unnatural, and limit the experimental paradigms that can be studied. Here, we describe a transformative MEG technology that can be worn on the head during movement. This opens up the possibility for non-invasive mapping of human electrophysiology across all ages and patient groups, with subjects who are free to move and interact with the real world.

At the core of our system is an array of optically pumped magnetometers (OPMs)—magnetic field sensors that rely on the atomic properties of alkali metals. These sensors have undergone marked development in recent years[2,3,6–9] and are well suited to MEG measurements[10–16]. In our system, each sensor contains a $3 \times 3 \times 3$-mm^3 glass cell containing ^{87}Rb vapour, which is heated to approximately 150 °C. A 795-nm circularly polarized laser beam, tuned to the D1 transition of rubidium, is used to spin-polarize the atoms, and the intensity of laser light transmitted through the cell is detected using a photodiode. In zero magnetic field, the spin magnetic moments align with the beam, and transmission of laser light to the photodiode is maximized. However, a magnetic field perpendicular to the beam causes Larmor precession, rotating the magnetic moments away from alignment. This causes a measurable drop in light transmission. The resulting effect is a zero-field resonance (Fig. 1b), which acts as a sensitive magnetic field indicator.

Each sensor is an integrated unit (Fig. 1c) with a noise level comparable to that of a superconducting quantum interference device (SQUID; about 15 fT per $\sqrt{\text{Hz}}$) and a dynamic range of ± 1.5 nT. Although the cell is heated, sensors can be mounted on the scalp because their external surfaces remain close to body temperature. Our prototype system (Fig. 1d)
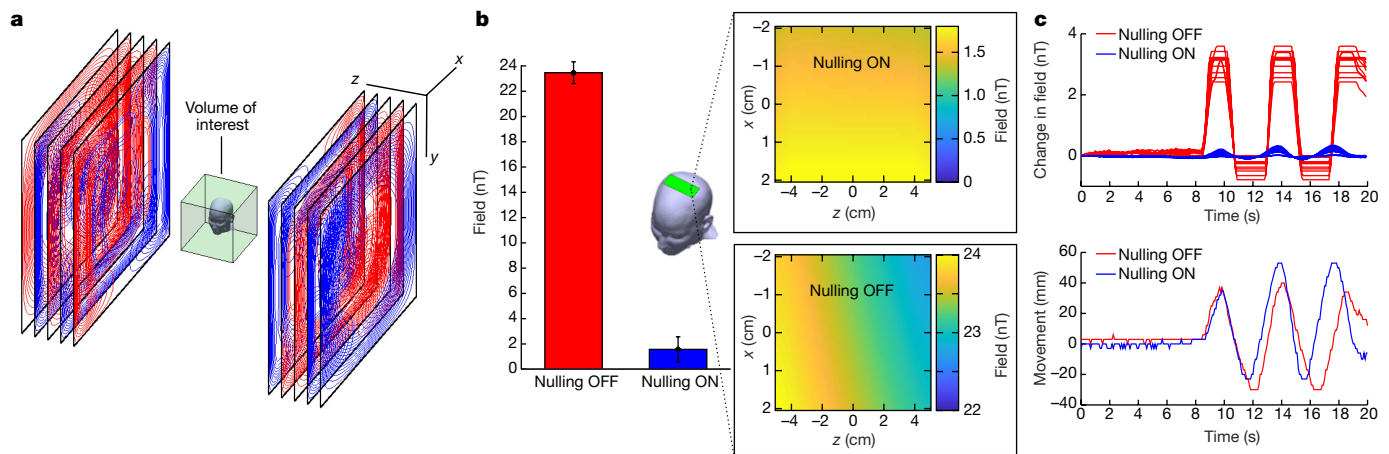
Figure 3 | Biplanar fingerprint-coil system for removing remnant static magnetic fields. a, Schematic of the coils, which are confined to two planes surrounding a $40 \times 40 \times 40$-cm^3 region of interest in which the head is allowed to move. The five separate layers represent wire paths that generate fields B_x, B_y, B_z, dB_x/dz and dB_z/dz. **b**, Bar chart showing field magnitude with and without field nulling. Inset images show spatial field variation of B_x. The static field was reduced from 23 ± 1 nT to 1.6 ± 1.0 nT. dB_x/dz measured across a 10-cm region spanning the width

of the head (green box in **b**) was reduced from 10 nT m^{-1} to 0.28 nT m^{-1}. **c**, Top, output of 13 OPMs over time while the subject nods their head (bottom, head movement). Blue and red traces show the cases where the field nulling system was on and off, respectively. Note that without field nulling the OPMs saturate during head movement, whereas with nulling the sensors continue to work, leaving an artefact that is comparable in magnitude to that due to an eye-blink.

comprised an array of sensors that were mounted in a 3D-printed 'scanner-cast'. The scanner-cast[12] was designed using an anatomical magnetic resonance imaging (MRI) scan, such that the internal surface snugly fits the subject's head, while the external surface accommodates the OPMs, which were positioned over the right sensorimotor cortex. Four additional reference sensors, sited near the subject's head, were used to measure background interference.

As a first demonstration, we measured electrophysiological activity in the right sensorimotor cortex during visually cued abduction of the left index finger. This task robustly elicits a reduction in endogenous beta band (13–30 Hz) oscillations during movement and a rebound (increase above baseline) following movement cessation[17]. Although simple, this task has been applied widely, with beta modulation being used as a marker of brain plasticity[18,19], psychosis[20,21] and white matter degradation[22]. A single experiment comprised 50 trials, each involving 1 s of finger abduction and 3 s of rest. Fifty 'dummy' trials (during which the subject did nothing) were interleaved to allow an estimate of baseline activity. A subject undertook the experiment twelve times: six during which they kept as still as possible, and six during which they made natural head movements, including nodding and shaking, stretching and drinking. Head motion was measured using an Xbox Kinect camera, which tracked the movement of three fiducial markers on the head. We also undertook the same static set of experiments using a cryogenic MEG system.

Figure 2 shows OPM-MEG data measured when the subject kept still (Fig. 2a) and moved (Fig. 2b). Subject motion is shown in the left-hand column. In the static case, motion was less than ± 1 cm, whereas in the moving case it exceeded ± 10 cm. The middle column shows images[23,24] of beta modulation (pink overlay) and the right-hand column shows a time–frequency spectrogram (TFS) of oscillatory change. In the TFS, blue indicates a decrease in oscillatory amplitude relative to baseline whereas red indicates an increase. Line plots of beta amplitude are shown in the inset. Equivalent data from the cryogenic system are shown in Fig. 2c, where movement was (necessarily) constrained to less than 2 mm. OPM-MEG performed consistently across experiments with the characteristic beta decrease and post movement rebound clearly delineated and localized to the sensorimotor cortex. Despite an order of magnitude increase in head movement, there was no significant difference in signal-to-interference ratio (SIR) between the moving and static runs ($P = 0.39$; two-sided Wilcoxon sum-rank test) and no correlation between the degree of movement and response

size (Extended Data Fig. 1 and Supplementary Information section 1). The spatial resolution of the OPM system was better than that of the cryogenic system, even with only 13 sensors (Extended Data Fig. 2 and Supplementary Information section 2). These data, along with a similar analysis of evoked responses (Extended Data Fig. 3 and Supplementary Information section 3), show clearly that the wearable system can be used to collect high-fidelity data even in the presence of large head movements.

Critical to the wearable MEG system is a means to null the background static magnetic field impinging on the OPMs. The system is housed inside a magnetically shielded room (MSR). However, the remnant Earth's field in the MSR is about 25 nT, and it is spatially inhomogeneous. Any sensor movement through this field during an MEG recording would result in a field change much larger than the fields of interest, and would exceed the narrow (± 1.5 nT) operational range of the OPMs, rendering them inoperable. In addition, such changes can modulate the sensor gain (Extended Data Fig. 4 and Supplementary Information section 4). To ameliorate this problem, we constructed a set of bi-planar electromagnetic coils designed to generate fields equal and opposite to the remnant Earth's field, thereby cancelling it out.

The coils were designed[25,26] on two 1.6×1.6-m^2 planes, placed either side of the subject with a 1.5-m separation (Fig. 3a). Three coils generated spatially uniform fields (B_x, B_y and B_z) while two additional coils were used to remove the dominant field variations (dB_x/dz and dB_z/dz). In this way, unlike standard field-nulling technologies (for example, tri-axial Helmholtz coils), our system can account for spatial variation of the field over a $40 \times 40 \times 40$-cm^3 volume of interest enclosing the head. Furthermore, we were able to cancel all components of the field vector using coils confined to just two planes, hence retaining easy access to the subject. Four reference OPM sensors were coupled to the coils in a feedback loop to null the residual static field in the volume of interest. We achieved a 15-fold reduction in the remnant Earth's field and a 35-fold reduction in the dominant field gradient (Fig. 3b). Figure 3c shows OPM measurements made during 7-cm head movements, with (blue) and without (red) field nulling. The results show that without field nulling, the OPM sensors failed (evidenced by the saturation). With field nulling, however, the OPMs were able to capture MEG data even while the head was moving (Supplementary Information section 5).

The ability to map human electrophysiology non-invasively, with whole brain coverage and high spatiotemporal resolution is, to our
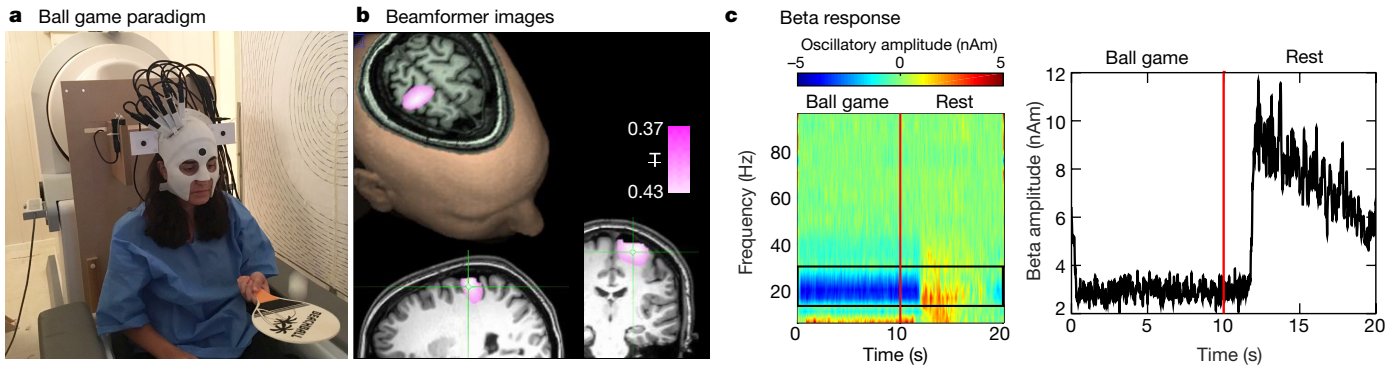
a Ball game paradigm   **b** Beamformer images   **c** Beta response

Figure 4 | An example 'real world' imaging paradigm. a, Experimental set-up: the seated subject continually bounced a table tennis ball off a bat for 10 s. This was followed by a 10-s baseline period, during which they did nothing. This was repeated 29 times. **b**, Spatial signature of beta band oscillatory change during periods of playing the ball game compared to rest. Note the difference in localization compared to Fig. 2, with the beta modulation localized to the arm and wrist area of sensorimotor cortex (distinct from the hand area in Fig. 2). **c**, Trial averaged time-frequency spectrogram (left) and amplitude of beta oscillations averaged over trials (right). The maximum head movement during this paradigm, assessed by the Kinect camera, was 6 cm.

knowledge, unique to MEG[27]. Alternative techniques either lack spatial specificity (for example, electroencephalography (EEG), which is also more susceptible to muscle artefacts (see Extended Data Fig. 5 and Supplementary Information Section 6)) or provide only indirect access to brain function via metabolic processes (for example, functional magnetic resonance imaging (fMRI)). However, current MEG systems exclude many subject cohorts and experimental paradigms. Our system represents a step change for functional imaging. A wearable instrument with scalp-mounted sensors means that subjects can be scanned at all ages, from babies to elderly patients, allowing imaging during key stages of cognitive development and decline. For example, it is well known that efficient communication between spatially separate cortical regions is key to healthy brain function, and that neural oscillations help to mediate such connectivity[28,29]. However, little is known about how electrophysiological brain networks emerge during the early years of life. Our system can characterize those networks, and the spectro-temporal profile of the connectivities that underlie them (see Extended Data Fig. 6 and Supplementary Information section 7). This highlights the potential utility of OPM-MEG for characterizing the developmental connectome.

A wearable system also opens doors to myriad neuroscientific investigations in which subjects can move naturally and interact with the real world. An example is given in Fig. 4, which shows brain activity elicited when the subject played a ball game (Fig. 4a). This naturalistic paradigm requires free, rapid and unpredictable head and arm movement; nevertheless, we were able to localize changes in beta oscillations to the arm and wrist area of motor cortex (Fig. 4b) and track the dynamics of oscillatory modulation (Fig. 4c). To evaluate the robustness of this measure, similar data were captured in two further subjects. Task-induced beta modulation, relative to baseline, was measured at 61%, 80% and 70% in the three participants. This simple example demonstrates the power of wearable neuroimaging to accurately assess brain function during a real world visuomotor coordination task, adding a new dimension to previous work[30]. This example could readily be extended to examine, for example, the neural correlates of motor coordination, their maturation during neurodevelopment and their breakdown in movement disorders. Such studies using naturalistic stimuli are inaccessible to conventional neuroimaging scanners owing to the movement required to undertake the task. In sum, this technology has transformative potential across a range of neuroscientific and clinical applications where knowledge of brain electrophysiology is informative.

Online Content Methods, along with any additional Extended Data display items and Source Data, are available in the online version of the paper; references unique to these sections appear only in the online paper.

1. Cohen, D. Magnetoencephalography: detection of the brain's electrical activity with a superconducting magnetometer. *Science* **175**, 664–666 (1972).
2. Kominis, I. K., Kornack, T. W., Allred, J. C. & Romalis, M. V. A subfemtotesla multichannel atomic magnetometer. *Nature* **422**, 596–599 (2003).
3. Shah, V. K. & Wakai, R. T. A compact, high performance atomic magnetometer for biomedical applications. *Phys. Med. Biol.* **58**, 8153–8161 (2013).
4. Hämäläinen, M. S., Hari, R., Ilmoniemi, R. J., Knuutila, J. & Lounasmaa, O. V. Magnetoencephalography: theory, instrumentation, and applications to non-invasive studies of the working human brain. *Rev. Mod. Phys.* **65**, 413–497 (1993).
5. Gross, J. *et al.* Good practice for conducting and reporting MEG research. *Neuroimage* **65**, 349–363 (2013).
6. Allred, J. C., Lyman, R. N., Kornack, T. W. & Romalis, M. V. High-sensitivity atomic magnetometer unaffected by spin-exchange relaxation. *Phys. Rev. Lett.* **89**, 130801 (2002).
7. Shah, V., Knappe, S., Schwindt, P. D. D. & Kitching, J. Subpicotesla atomic magnetometry with a microfabricated vapour cell. *Nat. Photon.* **1**, 649–652 (2007).
8. Dupont-Roc, J., Haroche, S. & Cohen-Tannoudji, C. Detection of very weak magnetic fields (10−9 gauss) by 87Rb zero-field level crossing resonances. *Phys. Lett. A* **28**, 638–639 (1969).
9. Borna, A. *et al.* A 20-channel magnetoencephalography system based on optically pumped magnetometers. *Phys. Med. Biol.* **62**, 8909–8923 (2017).
10. Alem, O., Benison, A. M., Barth, D. S., Kitching, J. & Knappe, S. Magnetoencephalography of epilepsy with a microfabricated atomic magnetrode. *J. Neurosci.* **34**, 14324–14327 (2014).
11. Alem, O. *et al.* Magnetic field imaging with microfabricated optically-pumped magnetometers. *Opt. Express* **25**, 7849–7858 (2017).
12. Boto, E. *et al.* A new generation of magnetoencephalography: room temperature measurements using optically-pumped magnetometers. *Neuroimage* **149**, 404–414 (2017).
13. Johnson, C., Schwindt, P. D. D. & Weisend, M. Magnetoencephalography with a two-color pump-probe, fiber-coupled atomic magnetometer. *Appl. Phys. Lett.* **97**, 243703 (2010).
14. Johnson, C. N., Schwindt, P. D. & Weisend, M. Multi-sensor magnetoencephalography with atomic magnetometers. *Phys. Med. Biol.* **58**, 6065–6077 (2013).
15. Kamada, K. *et al.* Human magnetoencephalogram measurements using newly developed compact module of high-sensitivity atomic magnetometer. *Jpn. J. Appl. Phys.* **54**, 026601 (2015).
16. Kim, K. *et al.* Multi-channel atomic magnetometer for magnetoencephalography: a configuration study. *Neuroimage* **89**, 143–151 (2014).
17. Pfurtscheller, G. & Lopes da Silva, F. H. Event-related EEG/MEG synchronization and desynchronization: basic principles. *Clin. Neurophysiol.* **110**, 1842–1857 (1999).
18. Gaetz, W., Macdonald, M., Cheyne, D. & Snead, O. C. Neuromagnetic imaging of movement-related cortical oscillations in children and adults: age predicts post-movement beta rebound. *Neuroimage* **51**, 792–807 (2010).
19. Mary, A. *et al.* Aging reduces experience-induced sensorimotor plasticity. a magnetoencephalographic study. *Neuroimage* **104**, 59–68 (2015).
20. Robson, S. E. *et al.* Abnormal visuomotor processing in schizophrenia. *Neuroimage Clin.* **12**, 869–878 (2016).
21. Uhlhaas, P. J. & Singer, W. Abnormal neural oscillations and synchrony in schizophrenia. *Nat. Rev. Neurosci.* **11**, 100–113 (2010).
22. Barratt, E. L. *et al.* Abnormal task driven neural oscillations in multiple sclerosis: A visuomotor MEG study. *Hum. Brain Mapp.* **38**, 2441–2453 (2017).
23. Brookes, M. J. *et al.* Optimising experimental design for MEG beamformer imaging. *Neuroimage* **39**, 1788–1802 (2008).

24. Van Veen, B. D., van Drongelen, W., Yuchtman, M. & Suzuki, A. Localization of brain electrical activity via linearly constrained minimum variance spatial filtering. *IEEE Trans. Biomed. Eng.* **44,** 867–880 (1997).
25. Poole, M. & Bowtell, R. Novel gradient coils designed using a boundary element method. *Concepts Magn. Reson. Part B Magn. Reson. Eng.* **31,** 162–175 (2007).
26. Carlson, J. W., Derby, K. A., Hawryszko, K. C. & Weideman, M. Design and evaluation of shielded gradient coils. *Magn. Reson. Med.* **26,** 191–206 (1992).
27. Baillet, S. Magnetoencephalography for brain electrophysiology and imaging. *Nat. Neurosci.* **20,** 327–339 (2017).
28. Brookes, M. J. *et al.* Investigating the electrophysiological basis of resting state networks using magnetoencephalography. *Proc. Natl Acad. Sci. USA* **108,** 16783–16788 (2011).
29. Hipp, J. F., Hawellek, D. J., Corbetta, M., Siegel, M. & Engel, A. K. Large-scale cortical correlation structure of spontaneous oscillatory activity. *Nat. Neurosci.* **15,** 884–890 (2012).
30. Jerbi, K. *et al.* Coherent neural representation of hand speed in humans revealed by MEG imaging. *Proc. Natl Acad. Sci. USA* **104,** 7676–7681 (2007).

Supplementary Information is available in the online version of the paper.

Author Contributions E.B.: system design and fabrication, data collection, data analysis, data interpretation, writing paper. N.H.: system design and fabrication, data collection, data analysis, data interpretation, writing paper. J.L.: system design and fabrication, data collection, data analysis, data interpretation, writing paper. G.R.: system design and fabrication, data collection, data analysis, data interpretation, writing paper. V.S.: system design and fabrication. S.S.M.: data interpretation, writing paper. K.J.M.: data collection, data analysis, data interpretation, writing paper. L.D.M.: data interpretation, writing paper. T.M.T.: data interpretation, writing paper. S.B.: data collection, data interpretation, writing paper. G.R.B.: conceptualization, system design and fabrication, data interpretation, writing paper. R.B.: conceptualization, system design and fabrication, data collection, data analysis, data interpretation, writing paper. M.J.B.: conceptualization, system design and fabrication, data collection, data analysis, data interpretation, writing paper.

METHODS

OPM-MEG system design and fabrication. *System overview.* An overview of our OPM-MEG system is shown in Extended Data Fig. 7a. The system comprised 13 OPM sensors (QuSpin), which were mounted on the scalp surface (the scalp array), and a further 4 sensors (placed close to the head, but not on the scalp surface) which were used to make reference measurements (the reference array). Each sensor produces an analogue voltage output that is proportional to the magnetic field perpendicular to the laser beam (scaling = 2.7 V nT^{-1}). The sensor outputs were digitized at a sample rate of 1,000 Hz, using a 16-bit digital acquisition (DAQ) system (National Instruments) controlled using custom-written software in LabVIEW. The sensor arrays were housed inside a magnetically shielded room (MSR) to reduce environmental magnetic interference; all control equipment was kept outside the room to minimize its effect on MEG measurements.

Prior to data acquisition, the reference array was used to identify the currents in the coils that best nulled the residual static magnetic field inside the MSR and its dominant first-order spatial variation. Reference sensors were located and oriented such that the three Cartesian components of the magnetic field (B_x, B_y and B_z), and the two dominant field gradients (dB_x/dz and dB_z/dz) could be measured close to the head (Extended Data Fig. 7b). Reference array measurements were input to a proportional integral derivative (PID) algorithm, which was used to control the currents in the field-nulling coils. This allows the calculation of currents which generate fields that are equal and opposite to those measured by the reference array, thus attenuating the static field over the volume spanning the subject's head. This step is key if the head is free to move during MEG data acquisition, as without field nulling, even small changes in head position or orientation (for example, a 4° rotation in a 25-nT field) would produce field variations large enough to render the OPMs inoperable (Fig. 3c).

During data acquisition, all 17 sensors (13 sensor scalp array and 4 sensor reference array) were operated simultaneously, with the reference sensors (which are sufficiently far from the scalp to be insensitive to the neuromagnetic field) used to characterize temporally varying background magnetic interference, which was later regressed from the signals recorded by the scalp-mounted sensors.

The visual cue for paradigm control was controlled by a separate stimulus computer. This was coupled to a data projector that projected the cue image through a waveguide onto a back-projection screen positioned ~40 cm in front of the subject. The stimulus computer also generated TTL trigger pulses of 1-s duration denoting the onset of the visual cues and the start of the rest periods. These trigger signals were input to the DAQ and sampled, simultaneously with the OPM data, at 1,000 Hz. Throughout data acquisition, an Xbox Kinect camera (Microsoft) was used to measure head movement. Video data were captured using a third computer, which also recorded the trigger channels so that movement data could later be analysed on a trial-by-trial basis.

OPM sensors. The fundamental building block of our system is the OPM sensor. We used compact commercially available sensors[3,11] (Fig. 1c), allowing a large number to be located flexibly on the scalp surface. Each OPM sensor head contains a semiconductor laser for optical pumping, optics for laser beam conditioning, a $3 \times 3 \times 3$-mm^3 ^{87}Rb vapour cell and a silicon photodiode for beam detection. The sensor head connects to a small electronics controller via a 5-m cable that is passed through a waveguide in the MSR. The sensor includes three on-board coils, which can be used to null static field components in the cell. Field changes (for example, due to neural currents in the brain) can be detected via the change in transmitted light intensity that they produce (Fig. 1b). The transmitted intensity shows a zero-field resonance, which is a Lorentzian function of the magnetic field components transverse to the laser beam, with a full width at half maximum of around 30 nT. For continuous field measurements, a sinusoidally modulated magnetic field of 1-kHz frequency is applied perpendicular to the laser beam using the on-sensor coils. The depth of modulation of the transmitted light, which is monitored using a lock-in process, is sensitive to the magnitude of the field component along the modulation axis[7,8]. The amplitude of the two field components perpendicular to the beam can be measured simultaneously by applying oscillating currents to two coils in quadrature. However, here only the radial field component was measured.

Scanner-cast design and 3D printing. Pre-recorded MRI and cryogenic MEG data were used to inform the design and construction of the individualized scanner-cast. To ascertain the shape of the subject's head, an anatomical MRI scan was acquired using a Philips 3T Ingenia MR system running a T$_1$-weighted gradient echo imaging sequence, with an isotropic resolution of 1 mm and a high bandwidth to limit field-inhomogeneity-related distortion. A 3D mesh, representing the outer surface of the head and face, was extracted from this image and then used to define a custom-fitted helmet, in which the OPM sensors could be mounted[12]. In a complete system, a large number of sensors would be spaced equidistantly across the entire scalp surface, giving whole brain coverage, but in our prototype system (used for the finger abduction and ball game paradigms), only 13 sensors were available and these had to be positioned for optimal coverage of the sensorimotor

region. To determine the optimal OPM sensor positions, we carried out the visually cued finger abduction experiment on the same subject using a cryogenic MEG system, and localized the source position and orientation using a beamformer. Having computed the location and orientation of the dipolar source, we used a forward model to compute the radial magnetic fields at the scalp surface generated by this dipole. The positions of the scalp-array sensors were then chosen to sample these fields optimally[12]. We assessed the effect of crosstalk between sensors, which may occur as a result of constructive interference of fields from adjacent sensors. For the sensor array used here we found these effects to be less than 3% when taking into account the radial field (Extended Data Fig. 8 and Supplementary Information section 8). See Supplementary Information section 7 for details of the scanner-cast that accommodated the 26 sensors that were used in a functional connectivity demonstration (Extended Data Fig. 6).

Field-nulling coils. The remnant Earth's field at the centre of our MSR is ~25 nT, and also shows significant spatial variation, with a gradient of ~10 nT m^{-1}. This means that translation through the inhomogeneous remnant field, or rotation with respect to the field vector, produces field changes at the sensors that are much larger than the neuromagnetic fields of interest (Fig. 3). Given the size of the remnant field and the narrow operational range of the OPMs (± 1.5 nT), such movement is likely to take the sensors outside their operational range. For example, a rotation of less than 4° in a field of 25 nT can produce a change of more than 1.5 nT in the amplitude of the magnetic field along an OPM sensor's sensitive axis, thus rendering it inoperable. The use of the field-nulling coils to reduce the remnant static (Earth's) field over a large central volume inside the MSR is therefore critical if the sensor array is to be operated without being rigidly fixed in position with respect to the MSR.

Here, the remnant field was nulled using a set of coils positioned on either side of the subject (see Fig. 3a). Five different bi-planar coils were constructed independently to null B_x, B_y and B_z and the two dominant field gradients dB_x/dz and dB_z/dz. In contrast to the tri-axial Helmholtz coil arrangement that is commonly used to null the remnant field inside an MSR, the bi-planar coil array allows cancellation of spatially varying fields and also does not significantly limit access to the subject, since the coil windings are confined to two vertical planes (rather than the three pairs of orthogonal planes that would enclose the subject when using three orthogonal Helmholtz coils). The bi-planar coil system therefore offers considerable advantages by eliminating the spatially uniform remnant field and its first-order spatial variation, while maintaining access to the subject.

Magnetic fields from bi-planar coils[31] were optimized for homogeneity using a harmonic minimization approach[26]. The current distribution *J* was confined to the two planes at $z = \pm a$ in the region $|x|,|y| < L$, and defined using the stream function *S* as $J = \nabla S \times \hat{z}$. *S* is parameterized as a two-dimensional Fourier series so that

$$S = \sum_n \left[\alpha_n \frac{\cos\left(n - \frac{1}{2}\right)\pi x}{L} + \beta_n \sin \frac{n\pi x}{L} \right] \times$$
$$\sum_m \left[\gamma_m \frac{\cos\left(m - \frac{1}{2}\right)\pi y}{L} + \delta_m \sin \frac{m\pi y}{L} \right]$$

Optimal values of the Fourier coefficients (α_n, β_n, γ_m, δ_m) were identified by exploiting the symmetry of the field distribution and then minimizing:

$$\sum_t [\boldsymbol{B}(\boldsymbol{r}_t) - \boldsymbol{B}_{target}(\boldsymbol{r}_t)]^2 + \omega P$$

Where $\boldsymbol{r}_t$ characterizes locations within the volume of interest at which a homogenous field or field gradient (described by $\boldsymbol{B}_{target}$) is required, and *P* represents the power dissipated in the coil. The coefficient ω can be used to adjust the weighting of the power term. Increasing ω reduces the complexity of the wire paths to be fabricated. $\boldsymbol{B}(\boldsymbol{r}_t)$ was calculated using the relationship

$$\tilde{\boldsymbol{B}} = \mu_0 \left\{ [ik_x\hat{\boldsymbol{x}} + ik_y\hat{\boldsymbol{y}}] \frac{\sinh}{\cosh}(k_r z) - k_r\hat{\boldsymbol{z}} \frac{\cosh}{\sinh}(k_r z) \right\} \tilde{S} e^{-k_r a}$$

where $\tilde{\boldsymbol{B}}$ and $\tilde{S}$ are the two-dimensional Fourier transforms of the field and stream function with respect to $x(k_x)$ and $y(k_y)$, and $k_r = \left(k_x^2 + k_y^2\right)^{\frac{1}{2}}$. The upper and lower sinh and cosh terms correspond to the case of the stream function having the same or opposite sign on the two planes. Coils were designed to produce a homogeneous (within ± 5%) field or field gradient over a $0.4 \times 0.4 \times 0.4$-m^3 central region, which is large enough to span the range of sensor positions during experiments in which head movement is allowed. The wire paths for each coil span an area of 1.6×1.6 m^2 and are layered on two planes of medium-density fibreboard separated by 1.5 m. The coil wire paths and contours of the magnetic field or field gradient in a central plane between the two coils are shown in Extended Data Fig. 9 for each coil. The

field variation was calculated by applying the elemental Biot–Savart law to the digitized wirepaths (see Supplementary Information section 5 for further discussion).

Motion detection and quantification. To quantify head movement, we used a simple optical tracking system based upon a Microsoft Kinect V1-2010 camera which was placed ~1 m in front of the subject. This camera provides a simultaneous 8-bit RGB video stream (640 × 480 pixel display, with 57° horizontal and 43° vertical field of view) and an 11-bit depth image, reconstructed from an infrared projected field. Data from both streams were captured using the MATLAB image acquisition toolbox, at 12 frames per second.

A motion-tracking algorithm was used to track the positions of three black dots on the outer surface of the white scanner-cast. The algorithm was initiated via manual selection of the three dots in the first frame of the video. A threshold detect routine then identified the dots and their centres of mass in all subsequent frames. Pixel numbers were converted to absolute locations in three dimensions by integrating the video data with the depth field. In this way, we defined parameters describing the motion of the three markers throughout the experiment. To quantify motion, movement parameters for all three orientations and all three fiducial locations were concatenated. Figure 2 (left) shows these data as a histogram plotted on a logarithmic scale.

Experimental method. *Finger abduction paradigm.* Experiments were carried out on a single subject (female, right-handed, age 27), who provided written informed consent (both to participation in the experiments and to release of photographs). The study was approved by the University of Nottingham Medical School ethics committee. The subject undertook multiple repeats of a visuomotor task[20]. The paradigm comprised visual stimulation with a centrally presented, maximum-contrast, vertical square-wave grating (3 cycles per degree). The grating subtended a visual angle of 8° and was displayed along with a fixation cross on a grey background. In a single trial, the grating was presented for 1 s followed by a 3-s baseline period during which only the fixation cross was shown. During presentation, the participant was instructed to make repeated abductions of their left (non-dominant) index finger. Fifty of these trials were recorded in each experiment. Blocks of ten trials were interspersed with blocks of ten 'rest' trials. In these rest trials (also 4 s in duration) the fixation cross remained on the screen, but no finger abduction was made. Averaging across the 50 'real' and 50 'rest' trials independently allowed assessment of SIR (see below). This experiment was repeated six times with the subject stationary and six times with the subject making natural movements. It was also repeated six times using a cryogenic MEG system.

The 'ball game' paradigm. The subject was seated in the OPM-MEG system and asked to play a simple ball game in which they continually bounced a table tennis ball on a bat. Ten-second bursts of 'ping-pong' were interspersed with 10 s of baseline activity (during which the subject was told to simply hold the bat and ball on their knee). This gave a total trial length of 20 s, and the subject repeated this 29 times. Owing to the location of the OPM sensors in the scanner-cast, the experiment was undertaken with the subject's non-dominant hand. Trials were cued by a second experimenter who was positioned inside the MSR throughout the experiment and gave verbal instructions to cue the game (they shouted either 'ping-pong' or 'rest' to begin or stop the game). This experiment was undertaken once in the OPM-MEG system by three subjects.

Cryogenic MEG system data acquisition. To compare OPM-MEG to cryogenic MEG recordings, we carried out the finger abduction experiment, in the same subject, using a 275-channel CTF MEG system (MISL) operating in third-order synthetic gradiometer configuration[32]. Data were acquired at a sampling frequency of 600 Hz and the subject was seated. Three electromagnetic position indicator coils were placed on the head as fiducial markers (at the nasion, left preauricular and right preauricular points). The locations of these fiducials were tracked continuously during the recording by sequentially energizing each coil and performing a magnetic dipole fit to these data. This allowed both continuous assessment of head movement throughout the measurement, and knowledge of the location of the head relative to the MEG sensors. Prior to the MEG recording, a 3D digitization of the subject's head-shape, relative to the fiducial markers, was acquired using a 3D digitizer (Polhemus). Co-registration of the MEG sensor geometry to the anatomical MR image was achieved by fitting the digitized head surface to the equivalent head surface extracted from the anatomical image. The subject undertook the experiment six times and a different head digitization was acquired each time.

Data processing: interference rejection. Following data collection, OPM-MEG data were processed to remove magnetic interference. The reference array sensors were located close enough to the scalp array to capture similar environmental interference, but sufficiently far away to be insensitive to the neuromagnetic fields of interest. This meant that the scalp and reference arrays could be used to synthesize a 'gradiometer' measurement whereby the scalp array data are de-noised

via regression of the reference array signals[12]. The reference array data from all four channels were combined in a single (design) matrix and a regression was used to remove any linear combination of reference array (interference) signals from the scalp array (neuromagnetic) signals. We applied this correction to the raw (that is, unfiltered) data.

Data processing: beamforming. Following interference rejection, all MEG data (OPM and cryogenic) were processed in the same way. Data were initially inspected visually, and any trials with excessive interference were discarded. This resulted in the loss of only one trial (from a cryogenic recording). A beamformer adaptive spatial filtering approach was then employed.

Using a beamformer[24,33], an estimate of electrical source strength $\hat{Q}_{\theta}(t)$ made at time t and a predetermined location in the brain is given by a weighted sum of sensor measurements such that

$$\hat{Q}_{\theta}(t) = W_{\theta}^T m(t) \qquad (1)$$

Here $m(t)$ is a vector of magnetic field measurements made at time t across all sensors (that is, 13 in our OPM system or 275 in the cryogenic system) and W_{θ} is a vector of weighting parameters tuned to a predefined location in source-space and current dipole orientation, represented by the vector θ. The superscript T indicates a matrix transpose.

The weighting parameters are derived on the basis of power minimization. The overall power in the output signal $\hat{Q}_{\theta}(t)$ is minimized with the linear constraint that power originating from the location and orientation of interest (θ) should remain. Mathematically, the beamformer problem can be written as:

$$\min_{W_{\theta}}\left[\hat{Q}_{\theta}^2\right] \text{ subject to } W_{\theta}^T L_{\theta} = 1 \qquad (2)$$

where $\hat{Q}_{\theta}^2$ represents the source power, given by $\hat{Q}_{\theta}^2 = W_{\theta}^T C W_{\theta}$, C represents the channel level data covariance matrix calculated over a time-frequency window of interest, and L_{θ} is the lead field vector, which is a vector containing a model of the magnetic fields that would be measured at each of the sensors in response to a source of unit amplitude with location and orientation θ. The (regularized) solution to equation (2) is found analytically to be:

$$W_{\theta}^T = [L_{\theta}^T\{C + \mu\Sigma\}^{-1}L_{\theta}]^{-1}L_{\theta}^T\{C + \mu\Sigma\}^{-1} \qquad (3)$$

Σ is a diagonal matrix representing the white noise at each of the MEG channels (which we approximate as the identity matrix) and μ is a regularization parameter[34]. Note that, in addition to source localization, the power minimization term has the desirable effect of reducing artefacts from, for example, muscles (Extended Data Fig. 10 and Supplementary Information section 9).

We sought to examine beta band effects, and so the beamformer weights were constructed, using equation (3), with covariance matrix C computed using beta band (13–30 Hz) data over a time window spanning the entire experiment[23] (400 s). In all cases (OPM and cryogenic MEG data) the regularization parameter was optimized to give the best SIR (defined as the standard deviation of the finger abduction trials divided by the standard deviation of the rest trials). The lead field was calculated using the analytical formulation first described by Sarvas[35]. Two other covariance matrices were constructed: C_a was defined as the data covariance in an 'active' window. This spanned the $0\,\text{s} < t < 1\,\text{s}$ window (relative to trial onset) in the case of the finger abduction paradigm, and the $1\,\text{s} < t < 9\,\text{s}$ window (relative to trial onset) in the ball game paradigm. C_c represented data covariance in a 'control' window ($1\,\text{s} < t < 2\,\text{s}$ for the finger abduction and $11\,\text{s} < t < 19\,\text{s}$ for the ball game). We then defined a pseudo-T-statistical contrast as

$$T_{\theta} = \frac{W_{\theta}^T C_a W_{\theta} - W_{\theta}^T C_c W_{\theta}}{2W_{\theta}^T C_c W_{\theta}}$$

Pseudo-T-statistics were computed at the vertices of a regular 4-mm grid spanning the entire brain. For each voxel, the orientation of each source was based on a non-linear search for the orientation that gave the maximum signal-to-noise ratio[33]. This method allowed construction of 3D images showing the spatial signature of maximum change in beta power. These images, averaged across experiments, are shown in Fig. 2 (middle) and in Fig. 4b.

Finally, to investigate the spectrotemporal signature of electrophysiological activity at the location of peak change, a time–frequency spectrogram (TFS) was derived. Here, the peak location/orientation, θ_{peak}, was extracted from the beamformer images, and a time course of electrophysiological activity for that location derived using equation (1) (the data covariance for the weights calculation was expanded to a broad (1–150 Hz) frequency range and covered the full 400 s of data collection). The resulting data were frequency filtered into 31 overlapping frequency bands, and a Hilbert transform was used to generate the amplitude

envelope of oscillations within each band. These envelope time courses were then averaged across trials, and experiments, and concatenated in the frequency dimension to generate a single TFS (shown in Fig. 2 (right) and 4c). The same method was used (with beta band filtered covariance for weights calculation) to examine beta band fluctuations.

Code availability. The MATLAB code used to analyse the current study is available from the corresponding author on request.

Data availability. The datasets generated during and/or analysed during the current study are available from the corresponding author on request.

31. Yoda, K. Analytical design method of shelf shielded planar coils. *J. Appl. Phys.* **67,** 4349 (1990).
32. Vrba, J. & Robinson, S. E. Signal processing in magnetoencephalography. *Methods* **25,** 249–271 (2001).
33. Robinson, S. & Vrba, J. in *Recent Advances in Biomagnetism* (eds Yoshimoto, T. *et al.*) 302–305 (Tohoku Univ. Press, 1998).
34. Backus, G. E. & Gilbert, F. The resolving power of gross Earth data. *Geophys. J. R. Astron. Soc.* **16,** 169–205 (1968).
35. Sarvas, J. Basic mathematical and electromagnetic concepts of the biomagnetic inverse problem. *Phys. Med. Biol.* **32,** 11–22 (1987).
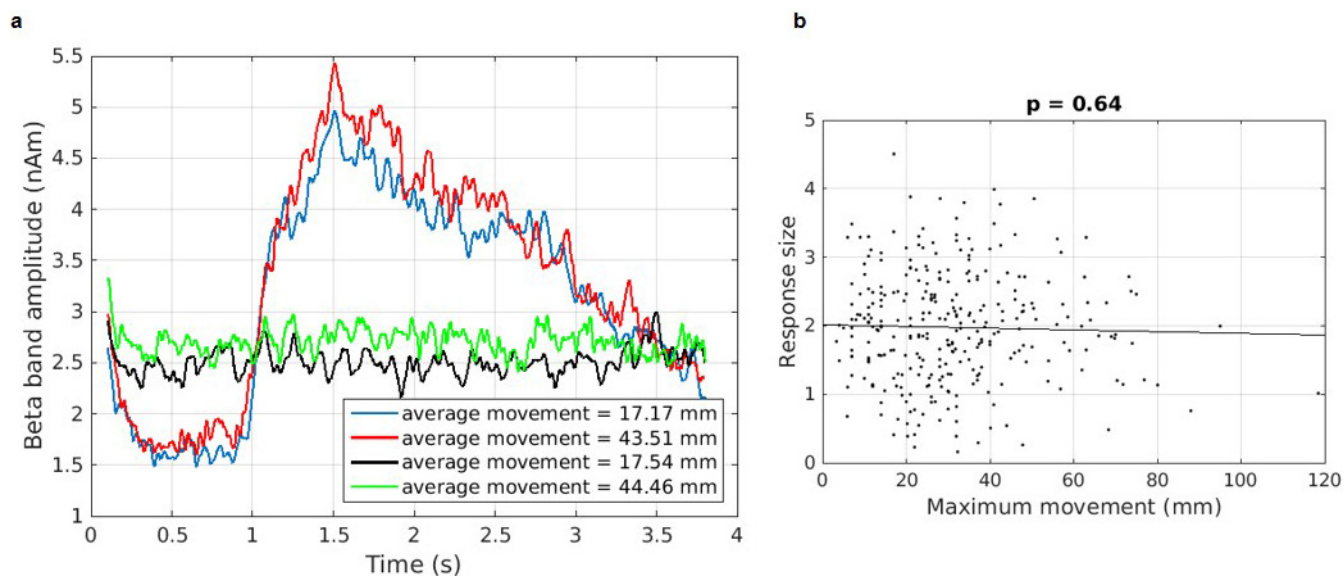
Extended Data Figure 1 | Response magnitude as a function of subject movement. a, Beta envelopes for finger abduction trials (blue/red) and resting trials (black/green) in the presence of large movement (red/green) and small movements (blue/black). **b**, The response size (that is, the difference between the mean amplitude during the desynchronization and rebound periods) shown as a function of maximum movement during a trial. Note that no measurable relationship was found. A significant ($P = 0.0052$, Pearson correlation) baseline shift was observed; this is likely to be a consequence of artefacts in the data generated by electrical activity in muscles controlling the naturalistic movements. See also Supplementary Information section 1.
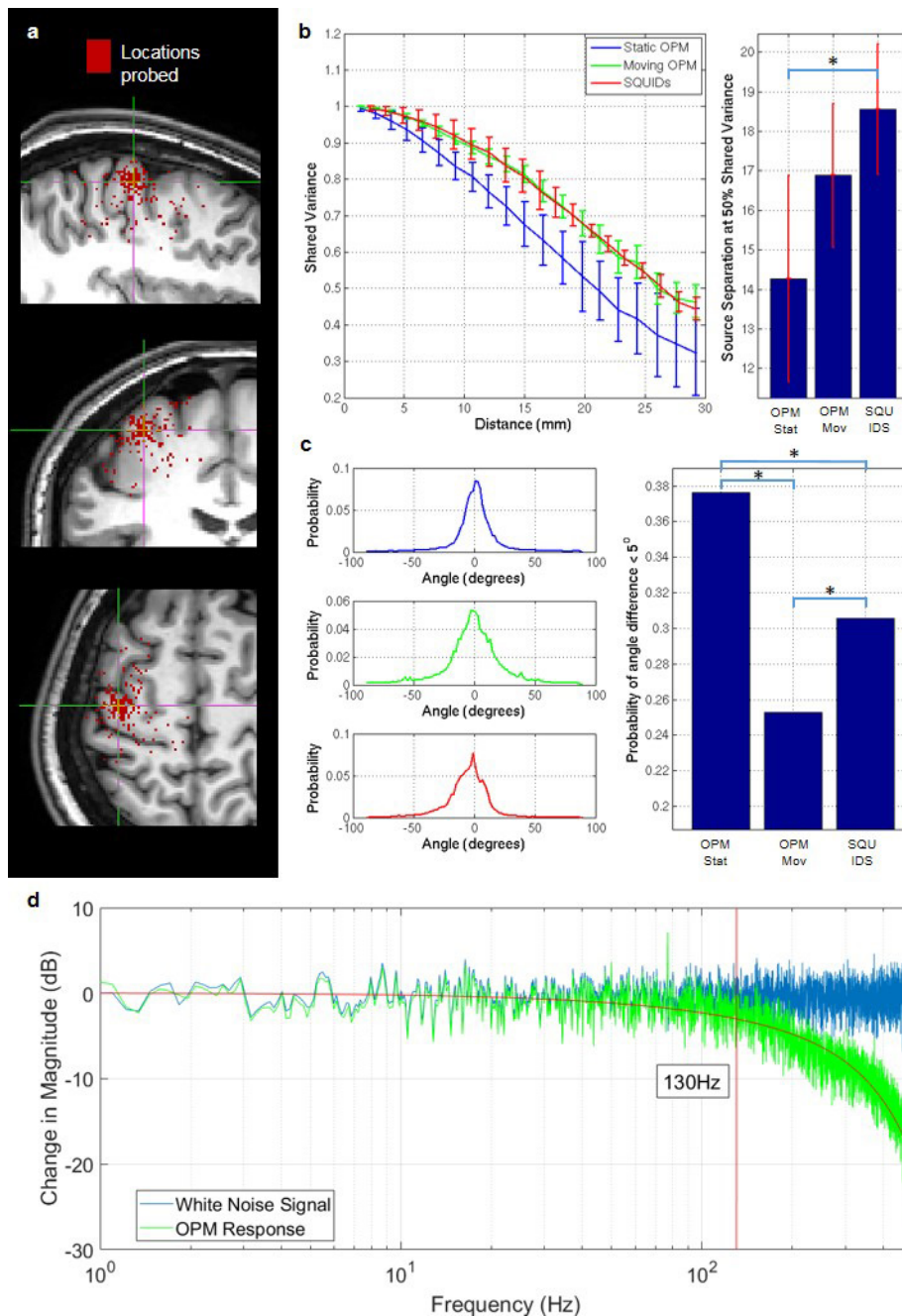
Extended Data Figure 2 | Quantification of spatial and temporal resolution. a, A 'seed' location was selected in sensorimotor cortex (at the cross-hairs). Four thousand random 'test' locations (red squares), within 3 cm of the seed, were selected randomly and probed. Shared variance was measured between electrophysiological time courses at the seed and test locations. **b**, Left, correlation between the seed and test time courses plotted as a function of spatial separation. Right, source separation at which shared variance dropped to below 50%. In both cases the error bars show s.d. over test locations. This serves as an absolute quantification of spatial resolution. Note that the OPM array, when static, significantly outperforms SQUIDs ($P = 0.002$, Wilcoxon sum-rank test). **c**, Quantification of the robustness of the source orientation estimation. While source power can vary between experiments, source orientation relies only on the local orientation of the cortical sheet, and should therefore be the same across equivalent experiments. Here the histograms show the source orientation difference (as an angle) across runs for 4,000 locations of interest. Note for all three experiments (static OPMs (top), moving OPMs (middle) and SQUIDs (bottom)) the probability distribution peaks at zero as would be expected. The bar chart shows the probability of observing an angular discrepancy below 5°; note

that the OPM array, when static, significantly ($P < 0.05$, permutation test) outperformed the SQUID array in terms of orientation robustness. Moving OPMs demonstrated the lowest robustness; however, this would be expected since the execution of natural movements differed across runs and therefore brain activity in the sensorimotor strip will also differ. The improvement in spatial specificity and robustness in our OPM-MEG system compared to a cryogenic (SQUID) system is likely to be a consequence of two factors: first, the closer proximity of the OPM sensors to the scalp provides higher signal-to-noise ratio in OPMs compared to SQUIDs; second, the scanner-cast ensures that, for each run, OPM sensors are in exactly the same location with respect to the brain. Cryogenic MEG, on the other hand, is subject to co-registration errors. **d**, Quantification of the OPM sensor's frequency response, which also defines its temporal resolution. An OPM sensor was placed in a Helmholtz coil and a white noise current source applied to the coil. The blue line shows the Fourier spectrum of the current source, the green line shows the spectrum of the measured field. Note that sensitivity falls by 3 dB at 130 Hz, giving a temporal resolution of 7.7 ms. See also Supplementary Information section 2.
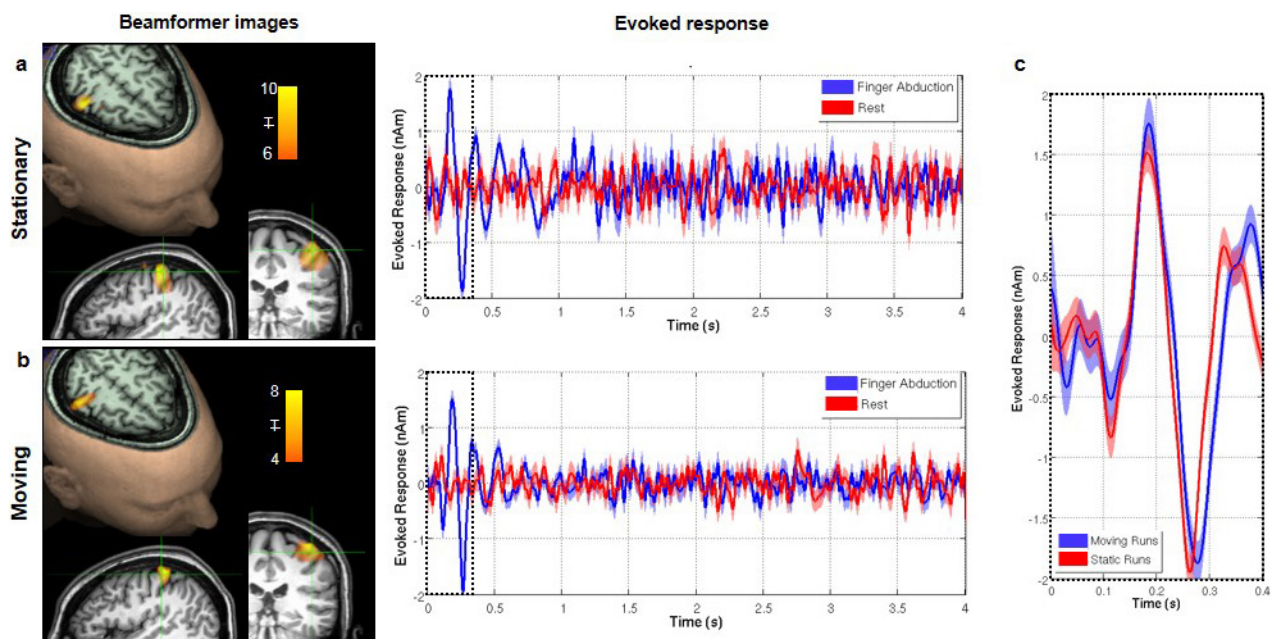
Extended Data Figure 3 | Evoked response analysis. a, Results when the subject was asked to remain still. **b**, Results when the subject was moving. Left panels show functional image: the overlay shows the spatial signature of the 2–30 Hz component of the evoked response, overlaid onto axial, sagittal and coronal slices of the anatomical MRI. Right panels show the time course of the evoked response; finger abduction trials in blue, rest trials in red. The shaded area shows standard error across six experiments. **c**, Direct comparison of the evoked response when the subject was asked to remain still (red) and was moving (blue). No significant SIR difference was found between static and moving runs ($P = 0.24$, two-sided Wilcoxon sum-rank test). See also Supplementary Information section 3.
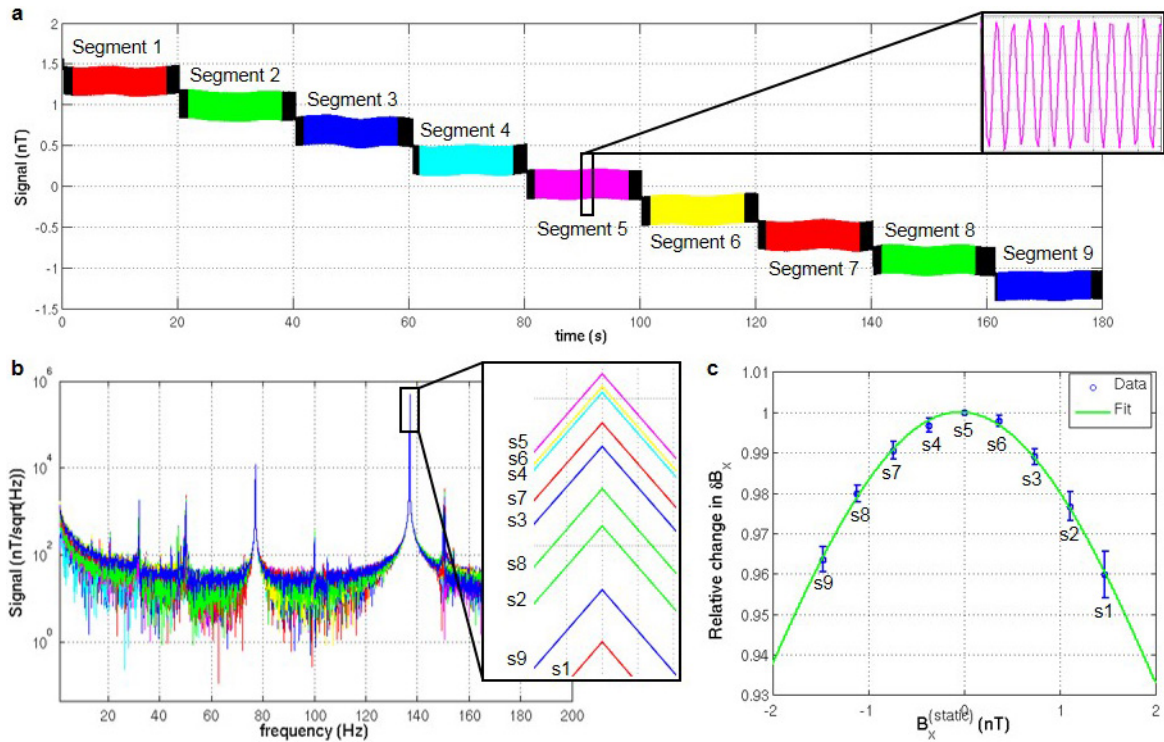
Extended Data Figure 4 | Gain changes with static magnetic field.
a, Raw OPM-MEG data recorded from a single channel during the gain experiment. Data were divided into nine segments (colour-coded here) corresponding to nine different static background magnetic fields ($B_x^{(static)}$), ranging between −1.5 nT and 1.5 nT. The inset plot shows the small oscillating field (δB_x), applied (in this sensor) at 137 Hz using the radially oriented on-sensor coil, which mimics neuromagnetic activity. **b**, Fourier transforms of each data segment. The inset figure shows the height of the 137-Hz peak for different segments. Note that the peak height changes as a function of static magnetic field. **c**, Fractional change in δB_x as a function of background field $B_x^{(static)}$. The blue circles show the measured data with the standard deviation over the six sensors. The green line shows a fitted Lorentzian function. See also Supplementary Information section 4.
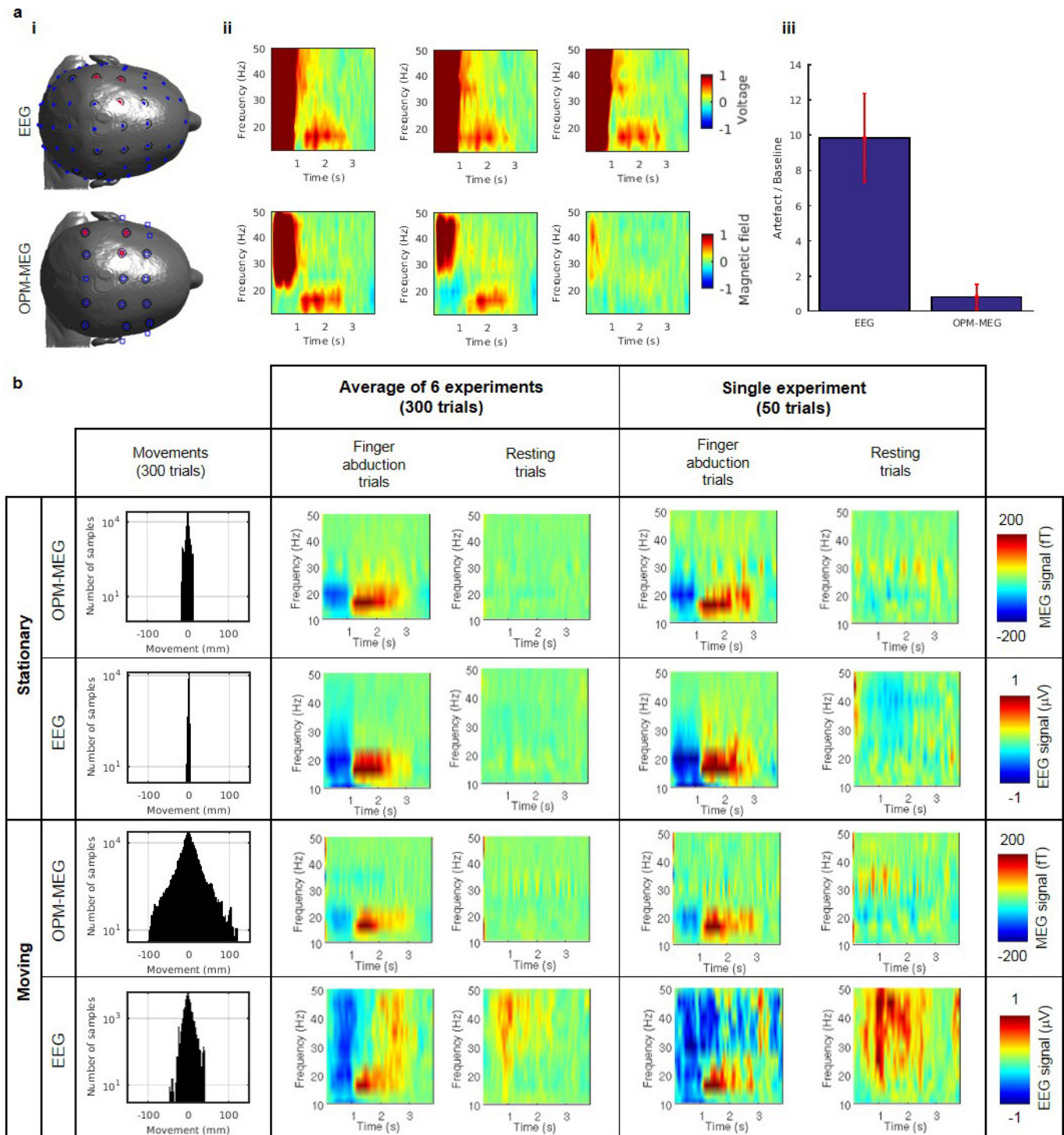
Extended Data Figure 5 | Comparison of EEG and OPM-MEG.
a, Muscle tensing experiment. i, Channel montages for EEG (top) and OPM-MEG (bottom). Blue circles show EEG channels used; blue squares show MEG channels used; red stars denote channels used to create (ii); black circles indicate channels used for averages in (iii). ii, Time-frequency spectra showing fractional change in oscillatory amplitude, relative to baseline. The three plots show three separate channels, with the muscle artefact visible in the 0–1-s window, when jaw clenching took place. iii, Quantitative analysis of the magnitude of the artefact, which was measured to be about ten times larger in EEG. Error bars show s.d. across sensors. **b**, Finger abduction experiment. The four rows show OPM-MEG and EEG data with the subject stationary, followed by

OPM-MEG and EEG data with the subject making natural movements. The left-hand column shows movement parameters. The left and left-centre time–frequency spectra show absolute difference from baseline of the MEG (in fT) and EEG (in μV) signals for individual channels, in the finger abduction and resting trials, respectively. These results have been averaged across all six experiments in both modalities. The right and right-centre time–frequency spectra show equivalent visualizations for a single representative experiment. Notice that, with the head stationary, MEG and EEG show similar results. However with the head moving, EEG data suffer from artefacts generated by muscle activity, to which the MEG data are less susceptible. See also Supplementary Information section 6.
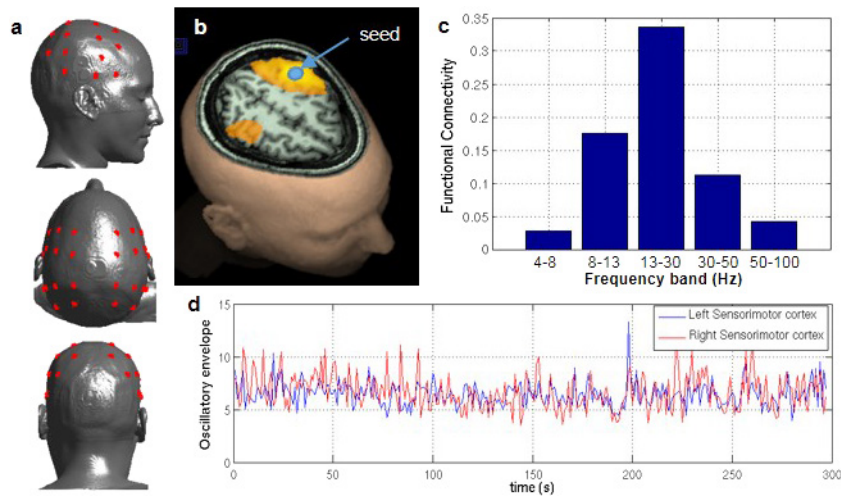
Extended Data Figure 6 | OPM-MEG derived functional connectivity.
A single subject took part in an experiment in which 5 min of OPM-MEG data were acquired in the resting state (subject was told to 'think of nothing'). The experiment was repeated twice and the results averaged. **a**, A 26-channel OPM scalp array, with OPM sensors positioned (using a scanner-cast) approximately to cover the left and right parietal lobes (red circles). MEG data were reconstructed in source space using a beamformer, on a 4-mm grid covering the entire brain. A seed location was selected in left sensorimotor cortex and functional connectivity between the seed and the rest of the brain computed using an amplitude envelope correlation measurement, with correction for signal leakage by regression. **b**, Regions exhibiting the strongest functional connectivity to the seed location (in the beta frequency band). Note that, in addition to a region around the seed, functional connectivity is observed in the homologous regions of the opposite hemisphere. This reflects long-range functional connectivity within the sensorimotor network. **c**, Functional connectivity strength between left and right primary sensorimotor cortex, plotted as a function of frequency. Note that, as expected, functional connectivity between these regions is greatest in the beta band (13–30 Hz). **d**, An example of beta band envelopes from the left (blue) and right (red) sensorimotor cortices, derived from resting state data. See also Supplementary Information section 7.
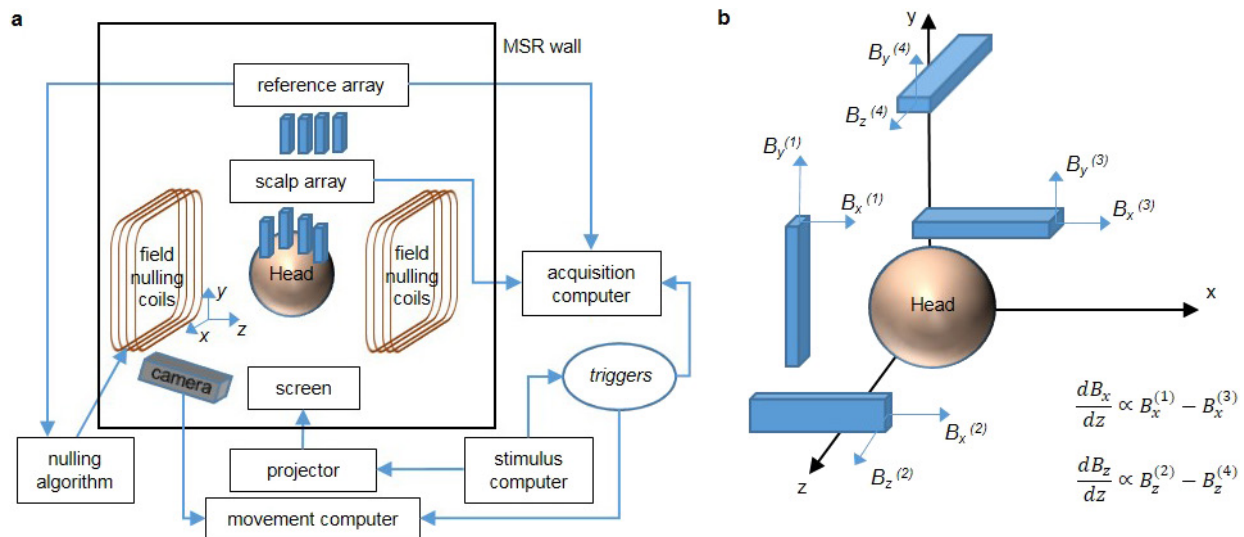
Extended Data Figure 7 | An overview of the OPM-MEG system.
a, Schematic showing an overview of system hardware. **b**, Positioning of the reference sensors relative to the head to allow measurement of the three Cartesian components of the magnetic field, and the two dominant spatial gradients of the field. Each sensor provides measurements of two components of the magnetic field that are perpendicular to the beam axis. Both components were measured for field nulling, but during experimental measurements only the component of the field along the long-axis of the sensor was measured.
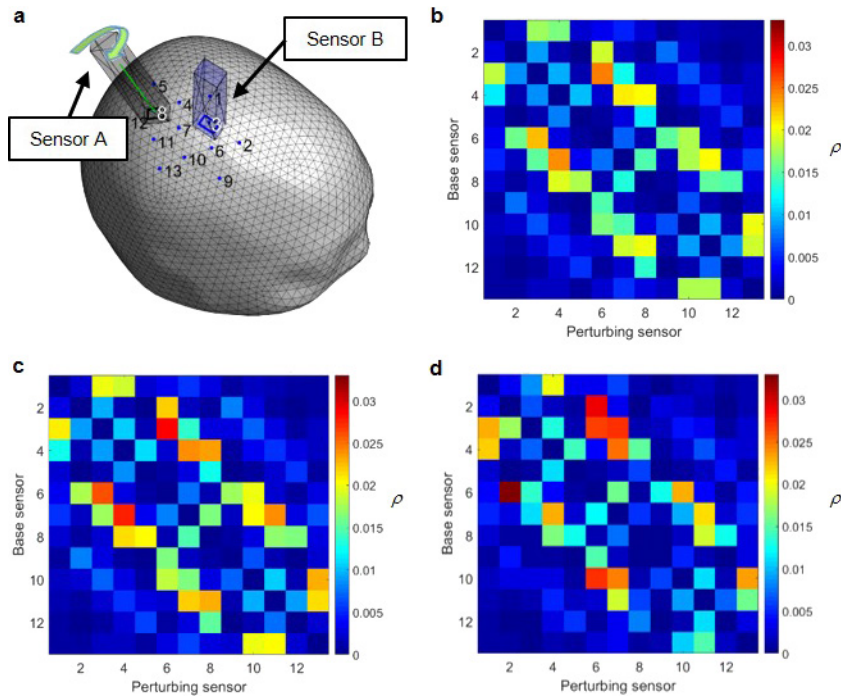
Extended Data Figure 8 | Crosstalk characterization across an OPM array. a, Schematic 3D representation of the crosstalk simulation. The head surface is shown with two example sensors. The locations of all 13 sensors are also indicated. We sought to characterize crosstalk between all pairs of sensors in the array. **b, c**, Simulated crosstalk between sensors measured as the ratio of fields generated by the perturbing sensor and the base sensor at the position of the base sensor. This ratio is a periodic function of sensor rotation about the radial orientation; the minimum interaction is shown in **b**, the maximum is shown in **c. d**, Experimentally measured crosstalk matrix. See also Supplementary Information section 8.
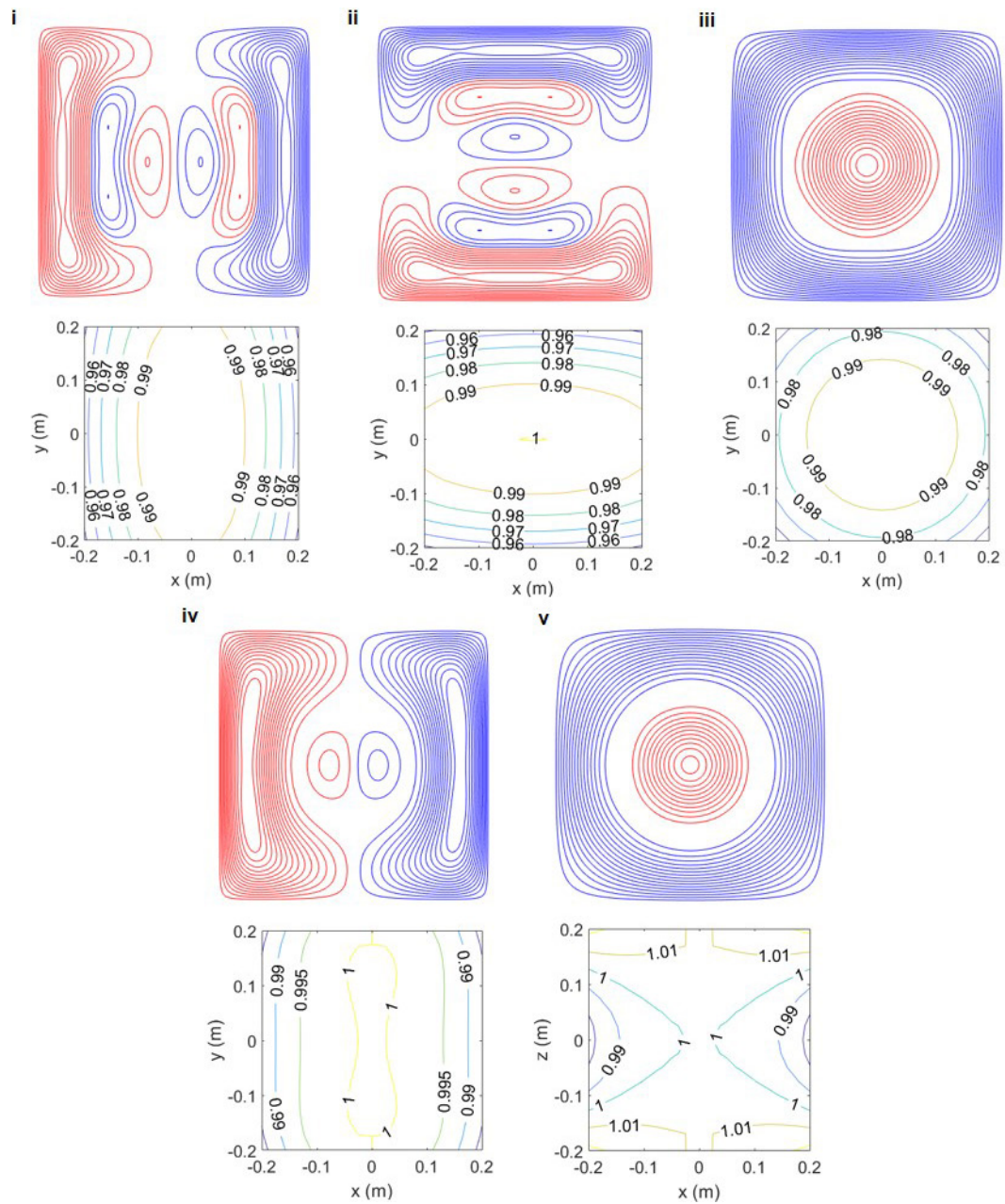
Extended Data Figure 9 | Coil designs. Wire paths and field plots are shown for the five coils: i, B_x; ii, B_y; iii, B_z; iv, dB_x/dz; v, dB_z/dz. The upper portion of each part shows the wire paths for one (1.6×1.6-m^2) plane of the bi-planar coil. Red and blue colours indicate clockwise and anticlockwise circulation of the current. The lower portion shows contours of the field or field gradient strength over the 0.4×0.4-m^2 x–y plane located at the centre of the volume of interest ($z = 0$). For v, contours are shown in the x–z plane at $y = 0$. The field or gradient values are normalized to the value at $x = y = z = 0$. Variation from the ideal field distribution is less than 5% over a $0.4 \times 0.4 \times 0.4$-m^3 central volume.
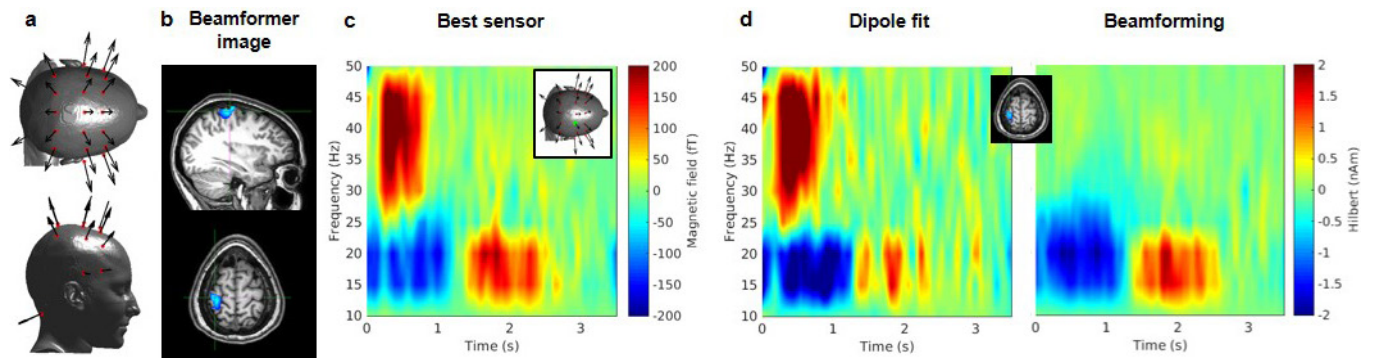
Extended Data Figure 10 | Removal of muscle artefacts via beamforming. a, The montage of OPM-MEG channels used to measure muscle artefact data. **b**, A beamformer image, highlighting a location of interest in right sensorimotor cortex. **c**, The time–frequency response for the best OPM-MEG sensor. **d**, Reconstructed responses from the over-regularized beamformer (which is analogous to dipole fitting) (left) and unregularized beamformer (right). Note that for unregularized beamforming the muscle artefact is supressed effectively. See also Supplementary Information section 9.

nature research

Corresponding author(s):   Matthew Brookes

☐ Initial submission   ☐ Revised version   ☒ Final submission

Life Sciences Reporting Summary

Nature Research wishes to improve the reproducibility of the work that we publish. This form is intended for publication with all accepted life science papers and provides structure for consistency and transparency in reporting. Every life science submission will use this form; some list items might not apply to an individual manuscript, but all fields must be completed for clarity.

For further information on the points included in this form, see Reporting Life Sciences Research. For further information on Nature Research policies, including our data availability policy, see Authors & Referees and the Editorial Policy Checklist.

▶ Experimental design

1. **Sample size**

   Describe how sample size was determined.

   > This is a proof of principle study to verify the operation of a new type of brain-scanner. For proof of principle of operation only a single subjected needed to be scanned

2. **Data exclusions**

   Describe any data exclusions.

   > No data excluded from analysis.

3. **Replication**

   Describe whether the experimental findings were reliably reproduced.

   > Our primary experiment (finger abduction), was replicated 6 times. All attempts at validation were successful. Our ball game experiment was repeated three times. Again, all attempts at validation were successfull.

4. **Randomization**

   Describe how samples/organisms/participants were allocated into experimental groups.

   > We have no groups so this is not applicable.

5. **Blinding**

   Describe whether the investigators were blinded to group allocation during data collection and/or analysis.

   > We have no groups so this is not applicable.

   Note: all studies involving animals and/or human research participants must disclose whether blinding and randomization were used.

6. **Statistical parameters**

   For all figures and tables that use statistical methods, confirm that the following items are present in relevant figure legends (or in the Methods section if additional space is needed).

n/a	Confirmed	
☐	☒	The exact sample size (n) for each experimental group/condition, given as a discrete number and unit of measurement (animals, litters, cultures, etc.)
☐	☒	A description of how samples were collected, noting whether measurements were taken from distinct samples or whether the same sample was measured repeatedly
☐	☒	A statement indicating how many times each experiment was replicated
☐	☒	The statistical test(s) used and whether they are one- or two-sided (note: only common tests should be described solely by name; more complex techniques should be described in the Methods section)
☒	☐	A description of any assumptions or corrections, such as an adjustment for multiple comparisons
☐	☒	The test results (e.g. P values) given as exact values whenever possible and with confidence intervals noted
☒	☐	A clear description of statistics including central tendency (e.g. median, mean) and variation (e.g. standard deviation, interquartile range)
☐	☒	Clearly defined error bars

   See the web collection on statistics for biologists for further resources and guidance.

▶ Software

7. Software

Describe the software used to analyze the data in this study.	All data analysed using custom written software in matlab.

For manuscripts utilizing custom algorithms or software that are central to the paper but not yet described in the published literature, software must be made available to editors and reviewers upon request. We strongly encourage code deposition in a community repository (e.g. GitHub). *Nature Methods* guidance for providing algorithms and software for publication provides further information on this topic.

▶ Materials and reagents

8. Materials availability

Indicate whether there are restrictions on availability of unique materials or if these materials are only available for distribution by a for-profit company.	No restrictions.

9. Antibodies

Describe the antibodies used and how they were validated for use in the system under study (i.e. assay and species).	N/A

10. Eukaryotic cell lines

a. State the source of each eukaryotic cell line used.	N/A
b. Describe the method of cell line authentication used.	N/A
c. Report whether the cell lines were tested for mycoplasma contamination.	N/A
d. If any of the cell lines used are listed in the database of commonly misidentified cell lines maintained by ICLAC, provide a scientific rationale for their use.	N/A

▶ Animals and human research participants

11. Description of research animals

Provide details on animals and/or animal-derived materials used in the study.	N/A

12. Description of human research participants

Describe the covariate-relevant population characteristics of the human research participants.	A single female subject, aged 27, took part in the primary study. Three individuals (2 male, 1 female) took part in the ball game experiment.